analytical chemistry

pubs.acs.org/ac Article

Microfluidic Chip for Cell Fusion and In Situ Separation of Fused Cells

Yaqi Bai, Chen Yang, Xiaoling Zhang, Jie Wu, Jun Yang, Huangxian Ju, and Ning Hu*

Cite This: *Anal. Chem.* 2024, 96, 19117−19125 Read Online

ACCESS | Metrics & More | Article Recommendations | Supporting Information

ABSTRACT: Electrofusion is an effective method for fusing two cells into a hybrid cell, and this method is widely used in immunomedicine, gene recombination, and other related fields. Although cell pairing and electrofusion techniques have been accomplished with microfluidic devices, the purification and isolation of fused cells remains limited due to expensive instruments and complex operations. In this study, through the optimization of microstructures and electrodes combined with buffer substitution, the entire cell electrofusion process, including cell capture, pairing, electrofusion, and precise separation of the targeted fused cells, is achieved on a single chip. The proposed microfluidic cell electrofusion achieves an efficiency of 80.2 ± 7.5%, and targeted cell separation could be conveniently performed through the strategic activation of individual microelectrodes via negative dielectrophoresis, which ensures accurate release of the fused cells with an efficiency of up to 91.1 ± 5.1%. Furthermore, the survival rates of the cells after electrofusion and release are as high as 94.7 ± 0.6% and 91.7 ± 1.2%, respectively. These results demonstrate that the in situ cell electrofusion and separation process did not affect the cell activity. This chip offers integrated multifunctional manipulation of cells in situ, and can be applied to multiple fields in the future, thus laying the foundation for the field of precise single-cell analysis.

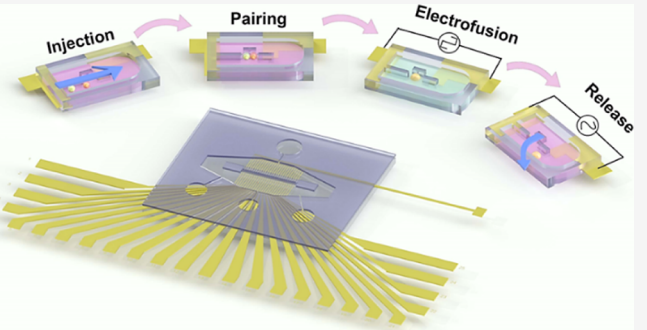

INTRODUCTION

Cell fusion technology can induce the transformation of two or more homologous or heterologous cells into hybrid cells, under in vitro conditions.[1,2] This technology has been extensively applied in various fields, such as immunomedicine,[3,4] drug delivery,[5,6] and gene recombination.[7,8] Common methods for cell fusion include chemical (e.g., polyethylene glycol, PEG),[9] biological (e.g., viral),[10] and physical (e.g., electrical induction, laser induction, etc.) approaches.[11,12] Among these methods, electrofusion has gradually become the most commonly used method due to its efficiency, controllability, and lower degree of cellular damage.[13]

In recent years, microfluidic chips have been widely used in biological analysis,[14] drug screening,[15] and clinical testing;[16] this is primarily due to their miniaturization, integration, low sample consumption, and high sensitivity.[17−19] Microfluidic chips also enable precise control of cells, facilitating efficient cell fusion. These advances have promoted the incorporation of cell electrofusion technology on microchips, significantly in recent years.[20,21] However, a challenge arises when separating fused cells. For example, in monoclonal antibody screening targeted hybridoma cells are often isolated through selective culture and subclone manipulation, which are time-consuming and laborious procedures.[22−24] Cytometry is also widely used to sort fluorescence-activated cells, but it requires specific instrumentation and specialized operations;[25,26] this makes efficient isolation of fused cells challenging, ultimately leading to a reduced utilization rate. Therefore, it is crucial to develop a simple on-chip separation technique of these cells for improve the efficiency and systematization of cell electrofusion chip technology, and ultimately promoting its widespread application.

Cell separation microfluidic chips have gained significant attention in recent years.[25−27] Abdulla et al. successfully achieved label-free isolation of circulating tumor cells (CTCs) based on cell size via a self-expanding focused microfluidic chip (SAIF), which could help predict cancer progression.[28] Shafiee et al. used contactless dielectrophoresis to selectively separate live human leukemia cells from dead cells based on differences in their electrical signals.[29] While these methods can effectively separate large quantities of cells, the precision and accuracy of individual cell separation are still unsatisfactory. To address this issue, Gan et al. developed an innovative microfluidic platform utilizing optoelectronic tweezers (OETs) that efficiently

Received: August 29, 2024
Revised: October 26, 2024
Accepted: November 12, 2024
Published: November 19, 2024

https://doi.org/10.1021/acs.analchem.4c04633
Anal. Chem. 2024, 96, 19117−19125

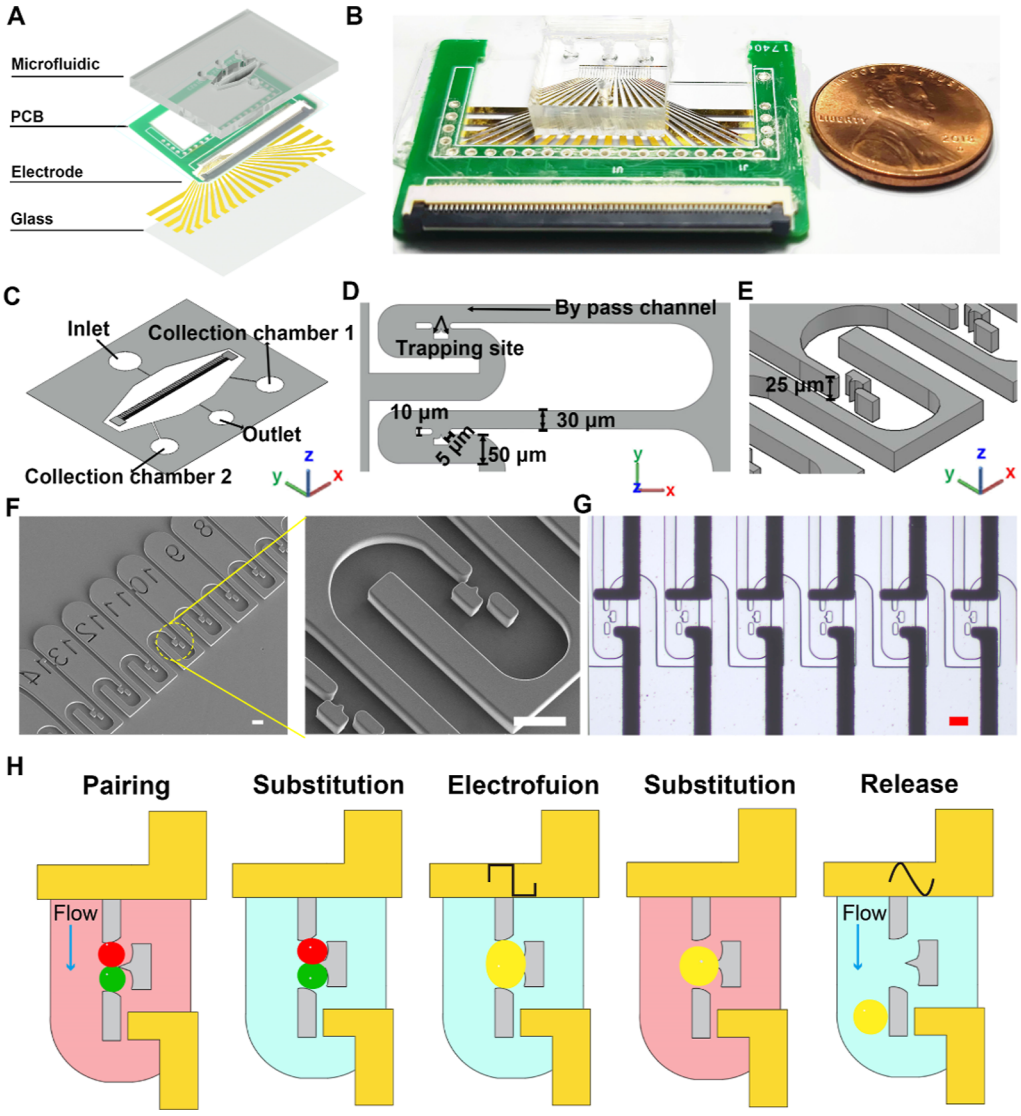

Figure 1. Microfluidic device for high-efficiency cell electrofusion and precise release of individual fused cells. (A) Composition diagram of the device. From top to bottom, there is a PDMS microfluidic chip layer, a PCB layer, a gold electrode layer and a quartz glass layer. (B) Image of the fabricated device. (C) Schematic illustration of the microfluidic structure. (D) Two-dimensional structure diagram (the xOy plane). (E) Three-dimensional structure diagram. (F) SEM image of the microchip. (G) Electrodes and microstructures under the microscope. (H) Scheme for cell pairing, electrofusion, solution substitution, and cell release. Scale bar: 50 μm.

captures and sorts single cells, enabling on-chip manipulation of single cells.[30] In addition, single-cell analysis microfluidic technology has achieved major breakthroughs in several key areas, including single-cell genomics,[31] proteomics,[32] drug screening,[33] and immunology.[34] While microfluidic technology has greatly enhanced the capabilities of single-cell analysis, integrating it with electrofusion technology remains challenging, particularly in achieving an electric field distribution suitable for both processes.

In this study, we introduce a new strategy for a simple microfluidic device, capable of efficiently performing the whole process of cell electrofusion on a chip, including cell pairing, electroporation, and in situ precise individual release. We designed and optimized the configurations of the cell capture unit and microelectrode to ensure that the distribution and parameters of flow/electric field meet the demands of both cell electrofusion and cell release. Cell capture was accomplished by hydrodynamic forces and while the cell electrofusion was induced by applying a high-intensity electric field. In addition, the fused cells were selectively released into the microfluidic channel and collection chamber, under the combined action of hydrodynamic force and negative dielectrophoresis (*n*DEP) force. Using this microfluidic device, on-chip proof-of-concept experiments have been conducted to demonstrate its capabilities for controlled cell pairing, reversible cell electroporation, and precise in situ release of fused cells. Finally, the effects of the above operations on cell viability were examined to evaluate their prospective application in cell electrofusion and correlative single-cell analysis.

EXPERIMENTAL SECTION

Microfluidic Chip Design. The microfluidic device comprises three layers: the PDMS microfluidic layer, the Au microelectrode arrays (MEAs), and the printed circuit board (PCB) adapter board, as depicted in Figure 1A,B. The PDMS microfluidic layer (Figure 1C) integrated an inlet and an outlet, facilitating the connection of the chip to a flow system. Additionally, two collection chambers were located on the

https://doi.org/10.1021/acs.analchem.4c04633
Anal. Chem. 2024, 96, 19117−19125

same side as the outlet for the collection of target cells (Figure 1C). The core of the microfluidic chip was consisted of 25 independent capture channels, and each channel contained a trapping site designed to capture and pair two cells. Given the cell size distribution of 10−20 μm, the width of these channels was set to 30 μm. To ensure effective cell trapping, the slit in the trap channel was 5 μm (Figure 1D). Furthermore, to prevent cell overlap at the trapping sites, the height of the chip was set to 23 μm (Figure 1E). Our structures feature a scale-filtering function: cells that are too large cannot be captured, whereas those that are too small may be missed, thereby ensuring that only cells of the appropriate size are captured.

The PCB served as the main control hub of the device, enabling precise individual addressing to achieve programmed cell separation. By applying a selective AC signal to the target microelectrodes, the device could induce the *n*DEP force to release the targeted cells. To facilitate single-cell release operations and simplify MEAs complexity, the MEAs were designed to consist of a common electrode and 25 individual control electrodes. Independent electrodes can electrically manipulate cells in each of the 25 channels for isolation of target fusion cells. These MEAs were coordinate-coded to facilitate subsequent manipulations (Figure S1). MEAs correspond to 25 independent capture channels, with electrode pairs spaced at a distance of 100 μm. We can enhance the throughput by replicating the existing capturing structure units and electrodes.

Device Fabrication. The SU-8 master was fabricated via standard photolithography. First, a layer of SU-8 photoresist, featuring a pillar height of 23 μm, was applied onto a silicon wafer by spinning at 3200 rpm for 30 s. Subsequently, the wafer underwent UV exposure through a glass mask. Following exposure, a development process and baking were performed. The formed SU-8 molds were subjected to a hard-baking process at 150 °C for 30 min, and the SU-8 master was vacuum-coated with 1*H*,1*H*,2*H*,2*H*-perfluorooctyl-trichlorosilane, creating a hydrophobic surface for smooth PDMS removal during molding. Subsequently, the PDMS, prepared by mixing the base and curing agent (Sylgard 184, Dow Corning) at a weight ratio of 10:1, was poured over the master mold. After eliminating residual bubbles by vacuum degassing and thermal curing (60 °C for 1 h), the PDMS slide with the desired microstructures was peeled away from the mold and cut into predetermined sizes and shapes. Finally, the microstructures were characterized by scanning electron microscopy (SEM) (Figure 1F).

The MEAs were fabricated on a quartz glass substrate by depositing a 5 nm thick Ti layer and a 100 nm thick Au layer via magnetron sputtering. First, the microelectrode patterns were created through a photolithography process using an AZ4620 photoresist. The exposed Ti and Au layers were subsequently wet etched away selectively using 1% HF and iodine (I_2) solutions, respectively. Next, the photoresist was removed to reveal the microelectrodes. Finally, the PDMS layer was accurately matched with the MEAs and irreversibly bonded to the quartz glass substrate (Figure 1G). Additionally, the assembled microfluidic chips could be subjected to secondary heat treatment (100 °C for 2 min) to strengthen bonding. Notably, based on prior experimental findings, under our specific experimental conditions, the PDMS would undergo a shrinkage of approximately 1%. Therefore, we scaled down the design size of the electrode by 1% in equal proportion to ensure a match with the contracted PDMS structure.

Cell Culture. The SP20 myeloma cell line was cultured in Roswell Park Memorial Institute (RPMI) 1640 medium (Gibco, Thermo Fisher Scientific, Waltham, MA, USA). The culture medium was supplemented with 10% Australian fetal bovine serum (FBS, Gibco, Thermo Fisher Scientific, Waltham, MA, USA), 1% penicillin/streptomycin (Biosharp, Hefei, China), 1% nonessential amino acids and 1% sodium pyruvate. The cells were maintained in a humidified incubator under a 5% CO_2 atmosphere at 37 °C. The SP2/0 cells were split at a ratio of 1:3 every 2 days, at an approximate cell density of 1×10^6 cells/mL by dilution with fresh cell culture medium.

Device Working Procedure. To prevent nonspecific protein adsorption, the chip was filled with a 1% bovine serum albumin (BSA) aqueous solution and incubated at room temperature (20−25 °C) for 20 min before cell loading. The experimental procedure for on-chip cell electrofusion and selective release of in situ fused cells includes five distinct steps: cell pairing, low osmolarity buffer substitution and cell swelling, reversible cell electroporation and electrofusion, RPMI 1640 solution substitution, and cell release (Figure 1H). First, the cells were introduced into the chip at a flow rate of 0.5 μL/min for 5 min, via a syringe pump. These cells were subsequently captured under hydrodynamic force and paired into the trapping site. After the cells paired in the majority of the trapping sites, cell-free fusion buffer (composed of 110 mM sorbitol, 0.1 mM calcium acetate, and 0.1 mM magnesium acetate) was loaded into the main channel at a flow rate of 0.5 μL/min for 10 min to wash away uncaptured cells, while displacing the RPMI 1640 buffer. The hypotonic buffer environment induces cells in trapping sites to swell, providing a stable microenvironment for cell electrofusion. And then, an appropriate direct-current (DC) electrical signal (amplitude: 10−18 V, pulse width: 8 μs, pulse interval: 1 s, number of pulses: 5) was applied. Following cell electrofusion, the RPMI 1640 medium was passed through as a solution substitution at a flow rate of 0.5 μL/min in the fourth step, which reduced potential cell damage (promoting cell viability) induced by a long incubation time in hypotonic buffer and provided an operating environment for *n*DEP. After approximately 10 min, because of o the difference in osmotic pressure, the cells lost osmotic water in RPMI 1640 and retracted to their normal sizes. Finally, the flow rate was adjusted to 0.2 μL/min, and an alternating-current (AC) electrical signal (frequency: 1 MHz, peak-to-peak voltage: 5 V_{pp}) was applied to release the target cell through the addressing operation.

The platform consisted of a fluorescence microscope (IX73, Olympus, Tokyo, Japan) and an Orca-ER CCD camera (IMG, China) to record the cell location information and experimental process, and a syringe pump (Pump11 PicoPlus Elite, Harvard Apparatus) for sample pumping.

Force Analysis and Finite Element Simulations. When a particle is exposed to a nonuniform electric field, it becomes polarized and an electric dipole is formed. Due to the nonuniform distribution of the electric field on both sides of the dipole, the particle is subjected to a force known as the dielectrophoretic (DEP) force. The time-averaged DEP force can be expressed as the following equation[35]

$$F_{DEP} = 2\pi\varepsilon_m r^3 \mathrm{Re}[K(\omega)]\nabla |E_{rms}|^2 \quad (1)$$

where ε_m is the permittivity of the medium, r is the radius of the spherical particle, $\nabla |E_{rms}|^2$ is the gradient of the root-mean-square of the electric field intensity, $K(\omega)$ is the Clausius−Mossotti (CM) factor, and $\mathrm{Re}[K(\omega)]$ represents its real part. If

https://doi.org/10.1021/acs.analchem.4c04633
Anal. Chem. 2024, 96, 19117−19125

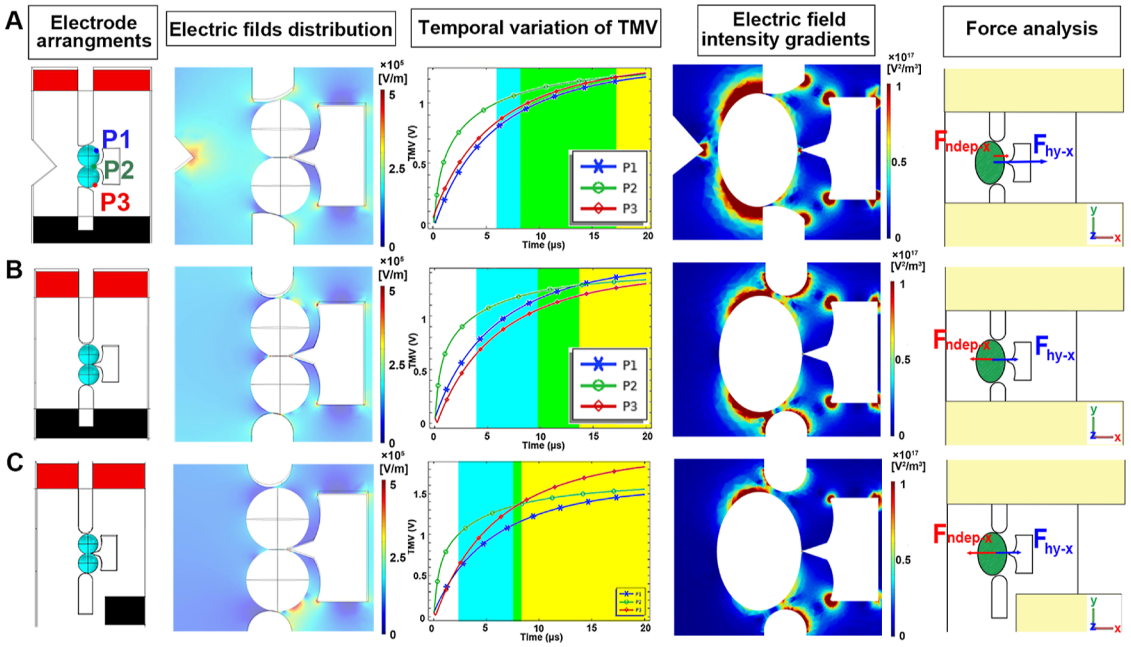

Figure 2. Simulations of the electric field distribution, gradient of the electric field intensity, temporal variation in TMV (the blue region indicates TMV that is suitable for cell fusion, the yellow part indicates that the pore size and pore density are suitable for cell fusion, and the green part where the blue and yellow regions cross indicates that cell fusion can be achieved), and analysis of forces during cell release for different electrode arrangements. Three configurations were explored. (A) In Configuration I, both the top and bottom electrodes are long and the microstructure contains a limit structure. (B) In configuration II, both the top and bottom electrodes are long. (C) In configuration III, the top electrode is long, whereas the bottom electrode is short.

$\mathrm{Re}[K(\omega)]$ is greater than 0, the particles are subjected to a positive DEP (pDEP) force, moving toward the region with a higher electric field intensity. In contrast, if $\mathrm{Re}[K(\omega)]$ is less than 0, they are subjected to a negative DEP (*n*DEP) force, moving toward the region with a lower electric field intensity.[36] $K(\omega)$ can be calculated via eq 2

$$K(\omega) = \frac{\varepsilon_p^* - \varepsilon_m^*}{\varepsilon_p^* + 2\varepsilon_m^*} \tag{2}$$

$$\varepsilon^* = \varepsilon - j\frac{\sigma}{\omega} \tag{3}$$

where ω ($\omega = 2\pi f$) is the angular frequency of the electric field and where ε^* is the complex permittivity. The subscripts p and m denote the particle and the suspension medium, respectively. ε and σ denote the permittivity and conductivity, respectively. Additionally, j is the imaginary unit with $j = \sqrt{-1}$. The real part of $K(\omega)$ varies from −0.5 to 1.[37] When $\varepsilon_p^* \gg \varepsilon_m^*$, $\mathrm{Re}[K(\omega)] \gg 1$, and $\mathrm{Re}[K(\omega)]$ tends to −0.5 when $\varepsilon_p^* \ll \varepsilon_m^*$.

When the target cells are released from the trapping site, they experience an *n*DEP force ($F_{n\mathrm{DEP}}$) within the xOy plane. This force, along with the hydrodynamic force (F_{hy}) generated by the fluid flow, affect the motion of the cell. Friction between the cells and the microstructure is neglected because the chip is treated with BSA to prevent specific adsorption. In actual experiments, the forces during particle motion are more complex and are briefly discussed here. For a spherical particle in a homogeneous medium, the hydrodynamic resistance it experiences in a fluid with a low Reynolds number can be expressed as[38]

$$F_{\mathrm{hy}} = 6\pi\eta r(v - v_p) \tag{4}$$

where η is the fluid viscosity, r is the particle radius, and v and v_p denote the fluid and cell velocities, respectively. When the fused cells are released from the trapping site, the *n*DEP force can overcome the hydrodynamic resistance, causing the cells to move toward the bypass channel under the combined effect of forces. The total force acting on the cell within the microstructure is calculated as

$$F_l = F_{n\mathrm{DEP}} - F_{\mathrm{hy}} \tag{5}$$

where F_{hy} denotes the hydrodynamic resistance to which the cells are subjected at the trapping site.

All the simulations were conducted in a 3-D model via COMSOL Multiphysics 5.6, and an example of a mesh independence test is shown in Figure S2. The steady-state Navier−Stokes equations for incompressible fluids were employed for the numerical simulation of the flow field during the cell pairing process. A difference in flow velocity was set between the inlet and outlet. The transmembrane voltage (TMV) distribution of the cell membrane was calculated via our previous electroporation modeling.[39]

RESULTS AND DISCUSSION

Microfluidic Design and Optimization. Both cell electrofusion and release necessitate accurate control of the electric field. Under the focusing effect of the microstructure on the electric field, a strong electric field constriction area is induced at the tip where the cells are in contact.[40] To achieve high-efficiency cell electrofusion and high cell viability, electroporation should be concentrated precisely on the cell contact surface, with minimal impact on the rest of the cell. The cells overcome the hydrodynamic force F_{hy} and rely on the *n*DEP force $F_{n\mathrm{DEP}}$ to move the cells toward the region with a lower electric field intensity gradient. To control this process accurately and efficiently, it is imperative to optimize the microstructure and electrode. The most important task is to

https://doi.org/10.1021/acs.analchem.4c04633
Anal. Chem. 2024, 96, 19117−19125

achieve a higher $\nabla |E_{rms}|^2$ with a low signal amplitude, which is essential for the efficient release of individual cells while minimizing any adverse effects on cell viability. Three configurations for the microstructure and electrode were considered (Figure 2).

According to the theory of electroporation, when the TMV reaches a sufficiently high value (~1 V), cell electroporation occurs.[41] In our device, efficient cell electrofusion occurs when all the following conditions are satisfied: the TMV of cells at P2 (Figure 2A) exceeds 1 V and is greater than that of cells at P1 and P3 (Figure 2A), the number of perforations is increased by 4 orders of magnitude compared with the initial value,[42] and the size of these perforations exceeds 60 nm.[41] Thus, we labeled different colors to represent various conditions in the temporal variation curves of TMV (Figure 2). The blue portion indicates that the value of TMV met the requirements necessary for electrofusion. The yellow portion signifies that both the pore density and pore radius fulfill the criteria for electrofusion. The green portion represents the achievement of simultaneous compliance with the requirements for both TMV and the pore density/pore radius, enabling electrofusion to proceed.

In addition, cell release only occurs when F_{nDEP} exceeds F_{hy} in the x-direction. To simplify the force analysis, we separately calculated $F_{nDEP\text{-}x}$ under an AC signal of 5 V_{pp} at 1 MHz, and F_{hy} at a flow rate of 0.2 μL/min, and the results of the calculations are shown in Table S1. The three-electrode and microstructure design schemes were shown in Figure 2A–C, corresponding to configuration I to III, respectively.

Configuration I (Figure 2A) results in highly efficient cell fusion, because its electroporation results in more aggregation at the cell contact point.[20] At an excitation voltage of 13 V, as illustrated in Figure 2A, cell electrofusion can be achieved with an 8.5–17.0 μs pulse width. However, the calculated forces indicate that $F_{nDEP\text{-}x}$ is 1.29×10^{-9} N and that $F_{hy\text{-}x}$ is 5.20×10^{-9} N. Force analysis reveals that the resultant force is directed toward the trapping site, thereby preventing cell release. Figure 2A shows a pronounced peak in electric field intensity gradient near the left tip. This high intensity can create challenges for cell release from the trapping site. Simultaneously, the arc-shaped sharp corner of the trapping site results in a significant electric field intensity gradient at its corner, thus making it difficult to escape the trapping site. Therefore, we need to optimize the electrode arrangement and structure to facilitate in situ cell electrofusion and precise cell release.

By modifying the arc of a sharp corner into a circular arc and removing the left tip (i.e., configuration II), the electric field intensity gradient is reduced (Figure 2B). This results in a weaker electric field focusing effect and therefore a larger excitation voltage for cell electrofusion. At an excitation voltage of 16 V, cell electrofusion can be achieved by using a pulse width of 9.6–13.5 μs. However, the calculated forces indicate that $F_{nDEP\text{-}x}$ is -1.85×10^{-9} N, $F_{hy\text{-}x}$ is 1.87×10^{-9} N, and the resultant force is also directed toward the trapping site, impeding cell release. Consequently, while this electrode arrangement facilitates cell fusion, it does not permit cell release.

The design of the asymmetric electrodes was introduced to induce a nonuniform electric field intensity gradient distribution for cell manipulation. Figure 2C shows the simulation results for configuration III, where the electrodes are longer at the top and shorter at the bottom. As the area directly opposite the electrodes decreases, the required excitation voltage increases. With an excitation voltage of 20 V, cell electrofusion can be achieved via a 7.4–8 μs pulse width. Furthermore, the calculated force $F_{nDEP\text{-}x}$ is -2.10×10^{-9} N, and $F_{hy\text{-}x}$ is 1.87×10^{-9} N, revealing that the resultant force in the x-direction is away from the trapping site. These findings demonstrate demonstrates that configuration III can simultaneously achieve cell fusion and in situ cell release. We also simulated the trajectories of the cells using this structure and electrode arrangement, and the results confirmed that the cells could be successfully released from the trapping site (Figure S3). Thus, configuration III was adopted in our study.

Cell Pairing and Electrofusion. To study the trapping process of cells within the structure, we simulated the fluid distribution at a flow rate of 0.5 μL/min. The cells were simplified to a rigid homogeneous sphere, as depicted in Figure 3A. The simulation results indicate that in the absence of cell capture (Figure 3A(i)), the fluid divides into three streams: one flows toward the bypass channel, another flows toward the left side of the trapping site and the third flows toward the right side. Under hydrodynamic force F_{hy}, cells are sequentially captured at the right and left trapping sites due to fluid resistance (Figure 3A(ii)). Once both trapping sites have captured cells (Figure 3A(iii)), the cells flow only along the bypass channel.

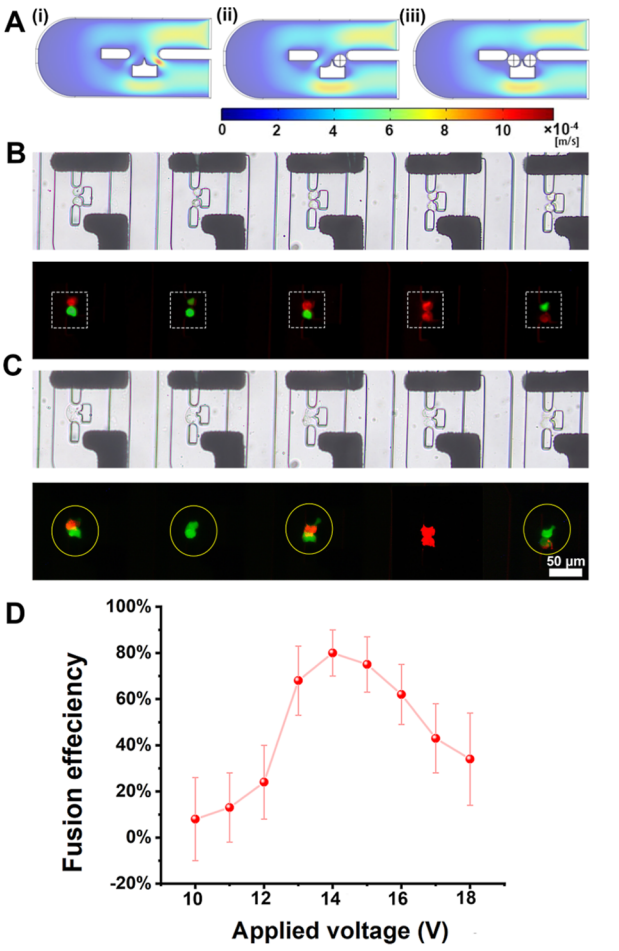

Figure 3. Cell pairing and electrofusion. (A). Flow field simulation with (i) no cell capture, (ii) one captured cell, and (iii) two captured cells at in the trapping site. (B) White light images and fluorescence images of cells before electrofusion (the dashed boxes indicate successfully paired cells). (C) White light images and fluorescence images of cells after electrofusion (solid circles indicate successfully fused cells). (D) Fusion efficiency at different electric field intensities.

https://doi.org/10.1021/acs.analchem.4c04633
Anal. Chem. 2024, 96, 19117–19125

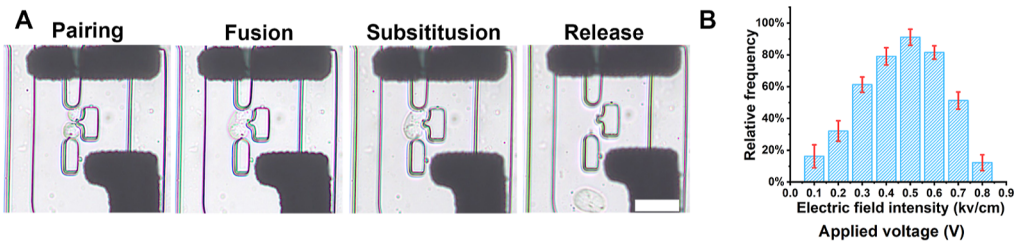

Figure 4. Complete fusion and in situ release process. (A) Process of cell release after electrofusion. Scale bar: 50 μm. (B) Statistics of the cell release efficiency at different voltages.

The flow rate plays a crucial role in the cell pairing process. The experimental results at different flow rates after pairing for 5 min are shown in Figure S4. When the flow rate was set at a high level of 0.8 μL/min, the cells were difficult to capture efficiently due to the high flow rate, and often escaped directly from the trapping site. The cell pairing efficiency at this time was 26.7 ± 6.1%. In addition, this high-speed flow may also because the cells to experience excessive shear force, which may adversely affect the viability of the cells. Conversely, if the flow rate was set to 0.2 μL/min, the pairing efficiency between cells was significantly reduced, making the pairing process sluggish and lengthy. This can lead to a prolonged residence time of the cells in a low osmotic pressure environment, again adversely affecting cell viability. The cell pairing efficiency at this point was 49.3 ± 8.3%. At 0.5 μL/min, the cells were be captured efficiently. The efficiency of cell pairing was 81.3 ± 2.3% when evaluated across 25 trapping sites. Specifically, the homologous (either red−red or green−green) cell pairing efficiency was 40.0 ± 4.0%, whereas the heterologous (red−green) cell pairing efficiency was 41.3 ± 2.3%. The structure facilitates efficient cell capture and pairing, as shown in Figure S5.

Following cell pairing, a buffer substitution procedure was executed. By introducing PM buffer with an osmotic pressure of 110 mOsm/kg of 0.5 μL/min for 10 min, the cells swelled due to the low osmotic pressure of the buffer, resulting in a tighter fit within the structure.[20] Immediately thereafter, a pulse DC signal was applied to induce cell fusion, as shown in Figure 3B,C, which demonstrate the changes before and after fusion. To provide a more detailed visualization of the fusion process, Movies 1 (white light) and Movie 2 (fluorescence) were recorded. Movie 2 specifically focused on the fusion of a green fluorescently labeled cell with an unlabeled cell, allowing for clear observation of the transfer of fluorescent substances. After the pulse DC signal was applied for approximately 20 s, the cell membrane at the cell junction ruptured, and green fluorescence began to flow from one cell into the other. After 40 s, the fluorescence intensities of the two cells lines were similar, which indicated significant merging of fluorescent components. After approximately about 1 min 10 s, a stable fusion cell formed, and the fluorescence did not change significantly. The fusion process revealed that reversible breakage of the cell membrane occurred only at the junction of the two cell lines, and no electroporation or cytoplasmic leakage was seen at the two poles of the cells.

Through comparative analysis, we found that the loaded pulse signal had a significant effect on the cell fusion efficiency. However, we also noted some differences between the simulation results and the experimental results; specifically, the excitation voltage for the simulation was slightly larger than that applied during the experiment. This disparity may stem from the combined effects of various factors such as environmental uncertainty, equipment accuracy and human operation. To explore the optimal electrofusion parameters, different voltage amplitudes were applied to the electrodes. Combining simulation and prior research, the cell electrofusion efficiency was statistically evaluated under specific conditions of a pulse width of 8 μs, 5 pulses, and a pulse interval of 1 s, and the fusion efficiency is defined in eq S1. The highest efficiency of 80.2 ± 7.5% was achieved at 14 V (Figure 3D), which demonstrated that this device exhibited a high cell fusion efficiency when the electrical parameters are appropriately set. Excessive voltage may adversely affect cell viability, resulting in a decrease in fusion efficiency, and Figure S6 shows the cell fusion process under an applied voltage of 8 V_{pp}. Conversely, a lower voltage may not create sufficient pore intensity or size on the contact surface.

In Situ Release of Fused Cells. After cell fusion, buffer substitution and in situ release of fused cells were executed, as illustrated in Figure 4A. Typically, cells are subjected to *n*DEP forces due to a negative Re$[K(\omega)]$ in RPMI 1640 medium that favors cell survival.[43] Therefore, RPMI 1640 medium was added for subsequent cell release processes. The smaller the frequency, the larger the value of Re$[K(\omega)]$. Theoretically, one should choose the smallest possible frequency for the experiment, but electrodes are prone to electrolysis in low frequency signals. Therefore, we chose a 1 MHz frequency for subsequent cell release.[44] Once the two cells were paired and fused at the trapping site, RPMI 1640 culture medium was added to the system at a controlled flow rate of 0.5 μL/min to ensure complete buffer substitution within approximately 10 min. This flow rate reduces the influence of shear stress on cell viability and prevents prolonged exposure of cells to low osmotic pressure. After buffer substitution, we adjusted the flow rate. Notably, in contrast to previous flow rate controls, the current flow rate serves only to prevent cell reflux. Relatively high flow rates necessitate the application of a greater voltage to achieve cell release. Therefore, a flow rate of 0.2 μL/min was utilized here.

Following buffer substitution, an electrical signal of 1 MHz and 1−8 V_{pp} was applied to the electrodes where the target cells were located. The resultant force, composed of both hydrodynamic force $F_{hy\text{-}x}$ and *n*DEP force $F_{n\text{DEP-}x}$, guided the cells toward the exterior of the trapping site, facilitating their release. Concurrently, the sample outlet was closed, and the collection chamber was opened. Once the cells were released, they were driven toward the collection chamber by the fluid and were ready to be further collected into Chamber 1 or 2 as needed. When there are different types of cells, e.g. homologous/heterologous cells, they can be collected in two separate collection chambers.

As shown in Figure 4B, we systematically analyzed the release accuracy of the cells under different applied voltages conditions. The statistical results reveal that the release accuracy initially increases and then tends to decrease with increasing voltage. Specifically, within the voltage range of 1 to 4 V, the *n*DEP force

https://doi.org/10.1021/acs.analchem.4c04633
Anal. Chem. 2024, 96, 19117−19125

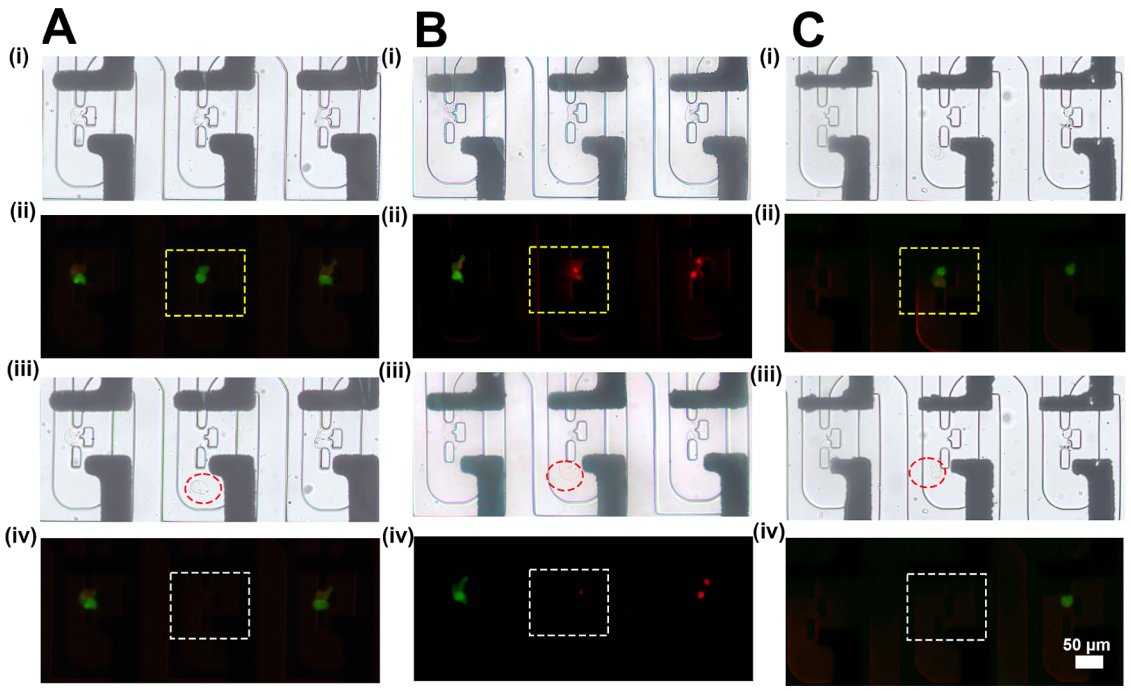

Figure 5. Controlled individual cell release. (A) Green−green fusion cells: (i) fused cells under white light and (ii) fluorescence, (iii) released cells under white light, and (iv) fluorescence image after cell release. (B) Red−red fusion cells: (i) fused cells under white light and (ii) fluorescence, (iii) released cells under white light, and (iv) fluorescence image after cell release. (C) Green−red fusion cells: (i) fused cells under white light and (ii) fluorescence, (iii) released cells under white light, and (iv) fluorescence image after release.

might not reach a sufficient threshold to effectively drive the cells away from the trapping site, resulting in a comparatively lower release accuracy. In contrast, when the voltage was increased to 6−8 V range, despite the significant enhancement increase in the *n*DEP force, the excessively strong electric field may have led to a decrease in cell activity and exacerbated the mutual interference of the electric fields among the different capture units (i.e., electric field crosstalk), resulting in a lower release accuracy (the release accuracy is defined in Equation S2). Notably, peak cell release accuracy is achieved at 5 V, up to 91.1% ± 5.1%, indicating that this voltage condition is ideal for achieving efficient and nondestructive cell release. Compared with existing cell sorting methods, this in situ separation strategy has great potential for high accuracy and convenience, which could improve and promote the application of cell fusion.

To access the effectiveness of the proposed configuration in mitigating electrical crosstalk between electrodes, thereby enabling individual cell release, we analyzed the situation of the cells surrounding the target cells. We positioned cells that had undergone green and red fluorescent labeling. Following pairing and fusion, we successfully achieved individual release of green−green fusion cells (Figure 5A), red−red fusion cells (Figure 5B) and red−green fusion cells (Figure 5C). Specially, a green−green cell located in the middle trapping site was designated the target cell (Figure 5A(ii)). The middle electrodes were energized at a frequency of 1 MHz and a peak-to-peak voltage of 5 V. As illustrated in Figure 5A(iii), the cell was released from the trapping site into the bypass channel, as marked by the red dashed box. Concurrently, the left and right cells remained in their original positions. The fluorogram in Figure 5A(iv) revealed that only the left and right cells exhibited fluorescence, confirming the absence of cells in the middle trapping site.

To verify the universality of the device, experiments were also conducted using red−red fusion cells and red−green fusion cells as target cells. In contrast to Figure 5A,B, although the red−green fusion is also a homologous cell fusion, the difference in color reflects the focus on different cell types in the experimental design. Figure 5C is unique in that it demonstrates the behavior of heterologous (red−green) fused cells. The results presented in Figure 5B,C confirm the successful independent release of both red−red and red−green fusion cells. These results is ensure that all types of target fusion cells can be individually released from the trapping site without affecting neighboring cells, in addition to further validating the device's ability to release target cells individually while maintaining the position of adjacent cells. The whole process of individual release of the target cells can also be found in Movie S3, demonstrating the effectiveness of our approach in achieving individual cell manipulation and release. In addition, although the process of cell-pairing in the chip is random, the implementation of our proposed selective release function provides a solid basic platform for cutting-edge fields, such as cellular homozygosity and heterozygosity histology analysis and gene integration difference studies.

In simulation analysis (Figure S7, the red and black rectangles symbolize the electrode ends), the results indicate that the maximum electric field intensity gradient at the tip of the microstructure PB was 1.8×10^{17} V^2/m^3, whereas that at the tips PA and PC was 7.3×10^{13} V^2/m^3, indicating a four-order-of-magnitude difference. This substantial difference suggests that our configuration effectively prevents electrical crosstalk between electrodes, facilitating the individual release of cells.

Cell Viability Investigation. To investigate the biocompatibility of the microfluidic device and ensure cell viability throughout the whole process, trypan blue dye was employed. This dye penetrates dead cells or those with significant membrane perforation, resulting in blue coloration. The cell

https://doi.org/10.1021/acs.analchem.4c04633
Anal. Chem. 2024, 96, 19117−19125

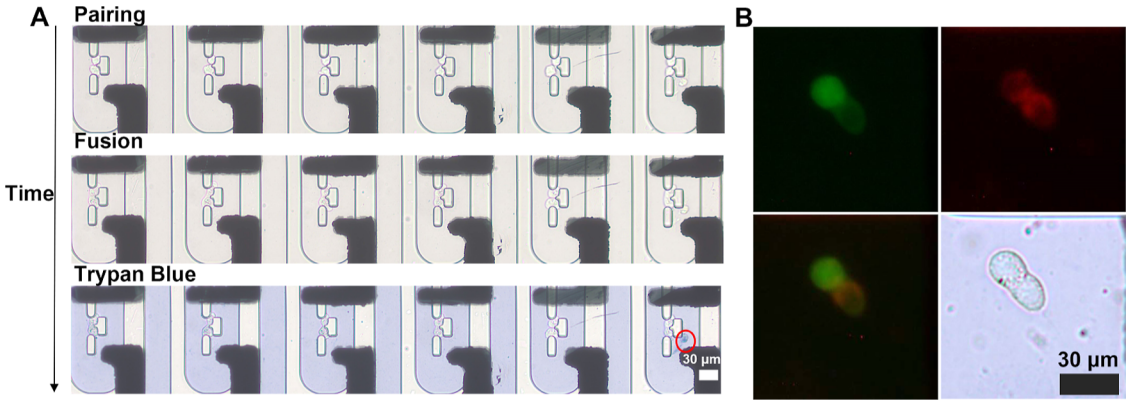

Figure 6. Cell viability test. (A) Timing diagrams of cell pairing, fusion, and trypan blue staining after fusion. (B) Images of the cells released under green fluorescence, red fluorescence, merged red and green fluorescence, and white light. Scale bar: 30 μm.

viability was accessed after the electrofusion and release processes separately. Figure 6A shows the cell electrofusion process, which involves cell pairing, the application of an electrical signal for fusion, and the addition of 1 μL of 0.4% trypan blue to evaluate cell viability. The results demonstrated no cell death at the trapping sites, yet cells within the red circles in the channel turned blue, potentially due to their preexisting poor condition, such as in the pairing process. The survival rate of the cells after electrofusion was 91.7 ± 1.2%. Concurrently, we tested the viability of the released cells. Since the released cells were not confined to a fixed microstructure and were therefore difficult to locate, the fused cells were released into the collection chamber. A fluorescence image revealed that the cells were a fusion of green and red fluorescent cells. Next, the cells were stained with trypan blue at a low flow rate (Figure 6B). Notably, there was no discoloration after staining, indicating that our device effectively performs an in situ cell release process without causing any damage to the cells. The survival rate of the cells after release was 94.7 ± 0.6%. These results clearly demonstrate that the adopted method results in low cell damage throughout the process, laying a solid scientific foundation for the in-depth application of this method in biomedical research, drug screening and other cutting-edge fields.

CONCLUSION

This work develops a microfluidic device for in situ fusion and individual cell release leverages efficient cell electrofusion techniques. By optimizing and adjusting the microstructure and electrode arrangement, with the aid of simulation analysis, the designed strategy can satisfy the requirements of both cell electrofusion and in situ independent release of fused cells. Using selective release, the fusion of nontarget cells is excluded, leading to more diverse and abundant fusion results. Under optimal electrical parameters, a cell electrofusion efficiency of 80.2 ± 7.5% was achieved. Additionally, precise and individual release of the target cells was achieved, with a release accuracy of 91.1 ± 5.1%. Moreover, the obtained cells exhibited good viability. This device can perform the functions of cell pairing, electrofusion, and independent release on a single chip with a simple operation process. This method addresses the significant challenge of poor fused cell separation and achieves low-damage, high-efficiency electrofusion, along with high accuracy in independent cell release. This fusion-separation multifunctional chip contributes significantly to the precise separation of fused cells, making it a powerful tool for single-cell manipulation and analysis.

ASSOCIATED CONTENT

Supporting Information

The Supporting Information is available free of charge at https://pubs.acs.org/doi/10.1021/acs.analchem.4c04633.

The design of electrodes, the example of mesh independence test, the trajectory of the cells when release from the trapping site, cell pairing at different flow rates, cell pairing in a large field of view, simulation and analysis of electric field crosstalk, the calculated forces of the cells, and the equations of fusion efficiency and release accuracy (PDF)

Cell electrofusion under fluorescence, Movie S1 (MP4)

Cell electrofusion under white light, Movie S2 (MP4)

Cell-independent release, Movie S3 (MP4)

AUTHOR INFORMATION

Corresponding Author

Ning Hu − *Key Laboratory of Biorheological Science and Technology, Ministry of Education and Bioengineering College, Chongqing University, Chongqing 400044, P. R. China;* orcid.org/0000-0002-6902-3302; Email: huning@cqu.edu.cn

Authors

Yaqi Bai − *Key Laboratory of Biorheological Science and Technology, Ministry of Education and Bioengineering College, Chongqing University, Chongqing 400044, P. R. China*

Chen Yang − *Key Laboratory of Biorheological Science and Technology, Ministry of Education and Bioengineering College, Chongqing University, Chongqing 400044, P. R. China*

Xiaoling Zhang − *School of Smart Health, Chongqing Polytechnic University of Electronic Technology, Chongqing 401331, P. R. China;* orcid.org/0000-0002-7412-2540

Jie Wu − *State Key Laboratory of Analytical Chemistry for Life Science, School of Chemistry and Chemical Engineering, Nanjing University, Nanjing 210023, P. R. China;* orcid.org/0000-0003-1379-122X

Jun Yang − *Key Laboratory of Biorheological Science and Technology, Ministry of Education and Bioengineering College, Chongqing University, Chongqing 400044, P. R. China;* orcid.org/0000-0001-6877-8677

Huangxian Ju − *State Key Laboratory of Analytical Chemistry for Life Science, School of Chemistry and Chemical Engineering, Nanjing University, Nanjing 210023, P. R. China;* orcid.org/0000-0002-6741-5302

Complete contact information is available at:
https://pubs.acs.org/10.1021/acs.analchem.4c04633

Notes

The authors declare no competing financial interest.

■ ACKNOWLEDGMENTS

This work was supported by the National Natural Science Foundation of China (nos 32071408, 21827812).

■ REFERENCES

(1) Chen, E. H.; Olson, E. N. *Science* **2005**, *308*, 369−373.
(2) Ramadan, R.; Vermeulen, L. *Cell. Mol. Gastroenterol. Hepatol.* **2021**, *11*, 304−306.
(3) Chan, Y. W.; So, C.; Yau, K. L.; Chiu, K. C.; Wang, X.; Chan, F. L.; Tsang, S. Y. *J. Cell. Physiol.* **2020**, *235*, 6794−6807.
(4) Li, Y.; Li, P. P.; Ke, Y. B.; Yu, X. Z.; Yu, W. B.; Wen, K.; Shen, J. Z.; Wang, Z. H. *ACS Appl. Mater. Interfaces* **2022**, *14*, 17128−17141.
(5) Sadeghian, F.; Hosseinkhani, S.; Alizadeh, A.; Hatefi, A. *Int. J. Pharm.* **2012**, *427*, 393−399.
(6) Zeng, Y.; Shen, M.; Singhal, A.; Sevink, G. J. A.; Crone, N.; Boyle, A. L. L.; Kros, A. *Small* **2023**, *19*, 2301133.
(7) Lobo, V.; Shcherbinina, E.; Westholm, J. O.; Nowak, I.; Huang, H.-C.; Angeletti, D.; Anastasakis, D. G.; Sarshad, A. A. *Sci. Data* **2024**, *11*, 617.
(8) Kuwabara, K.; Harada, I.; Matsuzawa, Y.; Ariizumi, T.; Shirasawa, K. *Hortic. Res.* **2021**, *8*, 250.
(9) Huang, L.; Chen, Y.; Huang, W.; Wu, H. K. *Lab Chip* **2018**, *18*, 1113−1120.
(10) Zhang, C. Y.; Meng, X. J.; Zhao, H. J. *Int. J. Mol. Sci.* **2022**, *23*, 7365.
(11) Ke, Q.; Li, C. X.; Wu, M.; Ge, L. P.; Yao, C.; Yao, C. G.; Mi, Y. *Bioelectrochemistry* **2019**, *127*, 171−179.
(12) Chen, S. X.; Cheng, J. P.; Kong, C. W.; Wang, X. L.; Han Cheng, S.; Li, R. A.; Sun, D. *Appl. Phys. Lett.* **2013**, *103*, 033701.
(13) Hu, N.; Yang, J.; Joo, S. W.; Banerjee, A. N.; Qian, S. Z. *Sens. Actuators, B* **2013**, *178*, 63−85.
(14) Song, X.; Yu, S.; Zhao, L.; Guo, Y.; Ren, X.; Ma, H.; Wang, S.; Luo, C.; Li, Y.; Wei, Q. *Anal. Chem.* **2022**, *26*, 9363−9371.
(15) Evans, B. R.; Beck, A. G.; Yeung, L.; Li, A.; Lee, D. H.; Bateman, K. P.; Chopra, G. *Anal. Chem.* **2024**, *96*, 488−495.
(16) Zhang, K.; Xi, J.; Wang, Y.; Xue, J.; Li, B.; Huang, Z.; Zheng, Z.; Liang, N.; Wei, Z. *Anal. Chem.* **2024**, *96*, 10092−10101.
(17) Whitesides, G. M. *Nature* **2006**, *442*, 368−373.
(18) Wang, Y. T.; Zhang, X. X.; Shang, L. R.; Zhao, Y. J. *Sci. Bull.* **2021**, *66*, 9−12.
(19) Li, L. J.; Wang, H. R.; Huang, L.; Michael, S. A.; Huang, W.; Wu, H. K. *Anal. Chem.* **2019**, *91*, 15908−15914.
(20) Bai, Y. Q.; Zhang, X. L.; Wang, X. F.; Xu, M. L.; Yang, J.; Hu, N. *Anal. Chem.* **2024**, *96*, 4437−4445.
(21) Kirschbaum, M.; Guernth-Marschner, C. R.; Cherré, S.; de Pablo Peña, A.; Jaeger, M. S.; Kroczek, R. A.; Schnelle, T.; Mueller, T.; Duschl, C. *Lab Chip* **2012**, *12*, 443−450.
(22) Li, X. Q.; Bian, H. F.; Yu, S. M.; Xiao, W.; Shen, J. Y.; Lan, C. F.; Zhou, K. N.; Huang, C. H.; Wang, L.; Du, D.; Lin, Y. H.; Tang, Y. *Anal. Chem.* **2018**, *90*, 2224−2229.
(23) Zhang, W. K.; Li, R.; Jia, F.; Hu, Z. Y.; Li, Q.; Wei, Z. W. *Lab Chip* **2020**, *20*, 4043−4051.
(24) Jin, Z.; Wang, L.; Cao, D.; Zou, S.; Chen, C.; Kang, H.; Song, Q.; Wang, H.; Tang, Y. *Anal. Chim. Acta* **2021**, *1163*, 338493.
(25) Kwizera, E. A.; Sun, M.; White, A. M.; Li, J.; He, X. *ACS Biomater. Sci. Eng.* **2021**, *7*, 2043−2063.
(26) Lin, S. J.; Zhi, X.; Chen, D.; Xia, F. F.; Shen, Y. H.; Niu, J. Q.; Huang, S. Y.; Song, J.; Miao, J. M.; Cui, D. X.; Ding, X. T. *Biosens. Bioelectron.* **2019**, *129*, 175−181.
(27) Wang, K. Y.; Zhou, W.; Lin, Z. G.; Cai, F. Y.; Li, F.; Wu, J. R.; Meng, L.; Niu, L. L.; Zheng, H. R. *Sens. Actuators, B* **2018**, *258*, 1174−1183.
(28) Abdulla, A.; Ding, X. *Methods Mol. Biol.* **2023**, *2679*, 207−218.
(29) Shafiee, H.; Sano, M. B.; Henslee, E. A.; Caldwell, J. L.; Davalos, R. V. *Lab Chip* **2010**, *10*, 438−445.
(30) Gan, C.; Zhang, J.; Chen, B.; Wang, A.; Xiong, H.; Zhao, J.; Wang, C.; Liang, S.; Feng, L. *Small* **2024**, *20*, 2307329.
(31) Luo, C.; Fernie, A. R.; Yan, J. *Trends Plant Sci.* **2020**, *25*, 1030−1040.
(32) Gebreyesus, S. T.; Siyal, A. A.; Kitata, R. B.; Chen, E. S.-W.; Enkhbayar, B.; Angata, T.; Lin, K.-I.; Chen, Y.-J.; Tu, H.-L. *Nat. Commun.* **2022**, *13*, 37.
(33) Lin, D.; Li, P.; Feng, J.; Lin, Z.; Chen, X.; Yang, N.; Wang, L.; Liu, D. *Small* **2020**, *16*, 1901001.
(34) Wang, C.; Qiu, J.; Liu, M.; Wang, Y.; Yu, Y.; Liu, H.; Zhang, Y.; Han, L. *Adv. Sci.* **2024**, *11*, 2401263.
(35) Khoshmanesh, K.; Akagi, J.; Nahavandi, S.; Skommer, J.; Baratchi, S.; Cooper, J. M.; Kalantar-Zadeh, K.; Williams, D. E.; Wlodkowic, D. *Anal. Chem.* **2011**, *83*, 2133−2144.
(36) Kung, Y. C.; Niazi, K. R.; Chiou, P. Y. *Lab Chip* **2021**, *21*, 1049−1060.
(37) Techaumnat, B.; Panklang, N.; Wisitsoraat, A.; Suzuki, Y. *Electrophoresis* **2020**, *41*, 991−1001.
(38) Torres-Castro, K.; Honrado, C.; Varhue, W. B.; Farmehini, V.; Swami, N. S. *Anal. Bioanal. Chem.* **2020**, *412*, 3847−3857.
(39) Xu, M. L.; Zhang, X. L.; Bai, Y. Q.; Wang, X. F.; Yang, J.; Hu, N. *APL Bioeng.* **2024**, *8*, 026103.
(40) Masuda, S.; Washizu, M.; Nanba, T. *IEEE Trans. Ind. Appl.* **1989**, *25*, 732−737.
(41) Li, C.; Ke, Q.; Yao, C.; Mi, Y.; Liu, H.; Lv, Y.; Yao, C. *PLoS One* **2018**, *13*, 0197167.
(42) Rems, L.; Usaj, M.; Kanduser, M.; Rebersek, M.; Miklavcic, D.; Pucihar, G. *Sci. Rep.* **2013**, *3*, 3382.
(43) Sadeghian, H.; Hojjat, Y.; Soleimani, M. *J. Electrost.* **2017**, *86*, 41−49.
(44) Kralj, J. G.; Lis, M. T. W.; Schmidt, M. A.; Jensen, K. F. *Anal. Chem.* **2006**, *78*, 5019−5025.